Article

UV-dark polar ovals on Jupiter as tracers of magnetosphere–atmosphere connections

Troy K. Tsubota [1] ✉, Michael H. Wong [2] ✉, Tom Stallard [3], Xi Zhang [4] & Amy A. Simon [5]

Aerosols in Jupiter's stratosphere form intriguing polar hoods, which have been investigated by ultraviolet cameras on Cassini and the Hubble Space Telescope. Transient, concentrated dark ovals of unknown origin have been noted within both the northern and southern polar hoods. However, a systematic comparative study of their properties, which could elucidate the physical processes active at the poles, has not yet been performed due to infrequent observations. Using 26 global maps of Jupiter taken by Hubble between 1994 and 2022, we detected transient ultraviolet-dark ovals with a 48% to 53% frequency of occurrence in the south. We found the southern dark oval to be 4 to 6 times more common than its northern counterpart. The southern feature is an anticyclonic vortex and remains within the auroral oval during most of its lifetime. The oval's darkness is consistent with a 20 to 50 times increase in haze abundance or an overall upward shift in the stratospheric haze distribution. The anticyclonic vorticity of the dark oval is enhanced relative to its surroundings, which represents a deep extension of the higher-altitude vortices previously reported in the thermosphere and upper stratosphere. The haze enhancement is probably driven by magnetospheric momentum exchange, with enhanced aerosols producing the localized heating detected in previous infrared retrievals.

Jupiter has been extensively studied using ultraviolet (UV) images from the Hubble Space Telescope (HST) and Cassini[1,2]. The polar regions are challenging to study, especially from Earth-based observations, because the high emission angles limit the spatial resolution. The polar regions are covered by stratospheric haze layers that are dark at UV wavelengths, which are called the the polar hoods[3]. These extend equatorward to 54° N and 62° S planetographic latitudes, respectively.

Discrete dark features inside the polar-hood boundaries were initially reported by ref. 4, who used HST Wide Field and Planetary Camera 2 (WFPC2) images in the 218 and 255 nm filters. These dark features were co-located with the auroral ovals, reinforcing the connection between dark polar aerosols and the auroral regions previously drawn from Voyager photopolarimeter 240 nm scans of the extended northern UV-dark polar hood and the more compact southern polar hood[5,6].

HST UV imaging data from 1997[7] and Cassini UV data from 2000[2] (Fig. 1a) revealed the discrete northern dark features to be oval in shape.

The Cassini northern UV-dark oval (NUDO) formed, evolved and decayed within the northern auroral oval during most of its lifetime between October and December 2000. However, Cassini did not detect a southern UV-dark oval (SUDO). We analysed UV images of Jupiter (Fig. 1) taken on 26 dates between 1994 and 2022 by HST/WFPC2 and HST Wide Field Camera 3 (WFC3) and found both NUDO and SUDO detections.

Results

Oval variability

HST observed the poles on 26 dates, as shown in Table 1, and we analysed all data that had full longitude coverage for the poles. Each pole

[1]Department of Physics, University of California, Berkeley, CA, USA. [2]Space Sciences Laboratory, University of California, Berkeley, CA, USA. [3]Department of Mathematics, Physics and Electrical Engineering, Northumbria University, Newcastle-upon-Tyne, UK. [4]Department of Earth and Planetary Sciences, University of California, Santa Cruz, CA, USA. [5]Solar System Exploration Division, NASA Goddard Space Flight Center, Greenbelt, MD, USA. ✉e-mail: tktsubota@berkeley.edu; mikewong@berkeley.edu
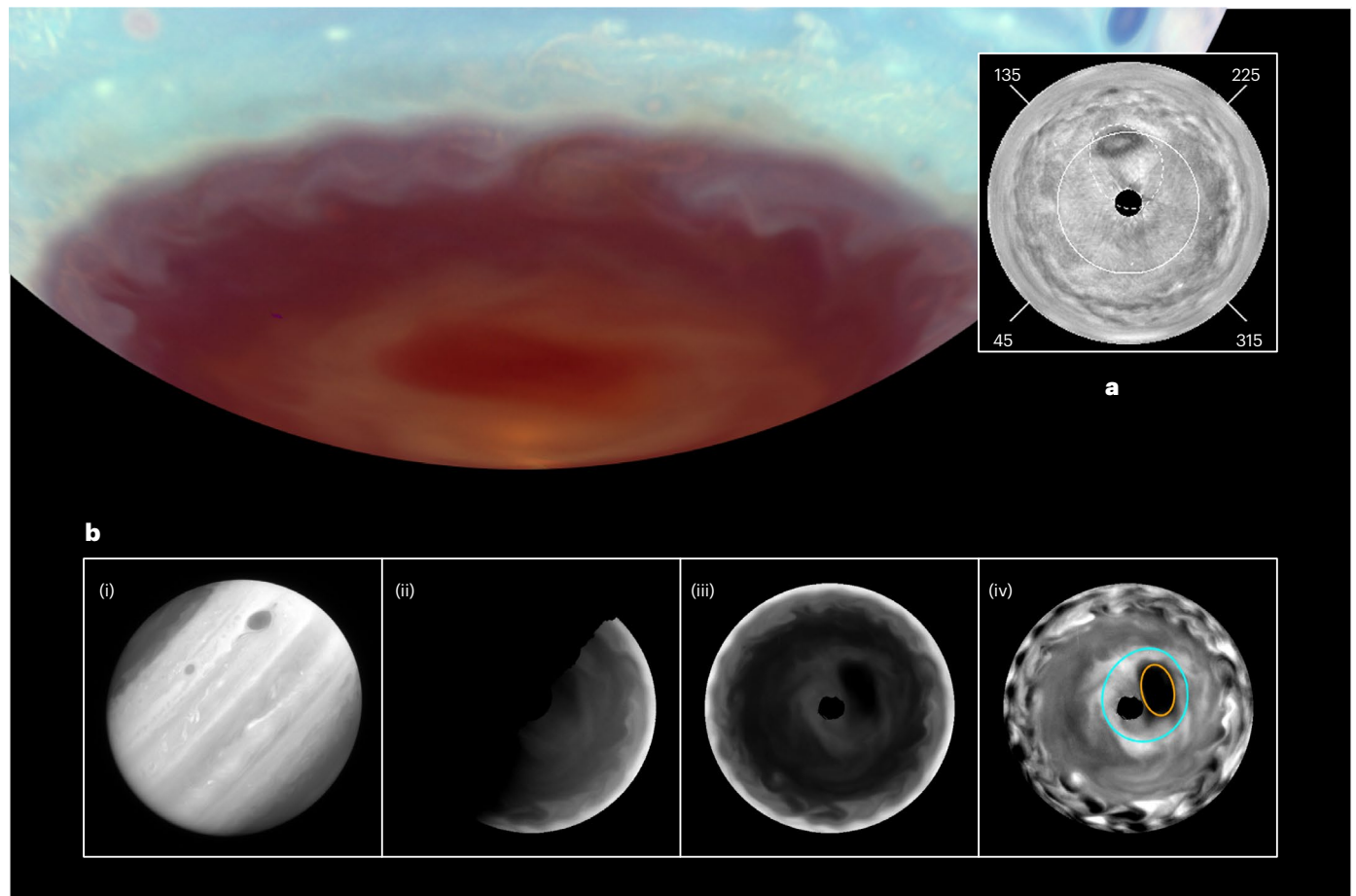
Fig. 1 | UDO in the south polar hood of Jupiter. Main image, 225 nm (R), 275 nm (G) and 343 nm (B) data were used for the composite. The bands were balanced to maximize the visibility of the dark oval. **a**, NUDO observed by Cassini in 2000, showing the main auroral oval (dashed) and the 60° N planetocentric latitude circle (solid). **b**, Steps in data preparation and analysis (Methods). (i) Navigated frame, (ii) orthographic polar projection, (iii) global polar mosaic (with limb-darkening correction), (iv) zonal average-subtracted polar mosaic with ellipse fit (orange border) and surrounding auroral oval (cyan border). Panel **a** reproduced with permission from ref. 2, AAAS.

was observed on 25 dates. South polar maps for the 15 HST/WFC3 observation dates are shown in Fig. 2. North polar maps of HST/WFC3 observations and polar maps for HST/WFPC2 observations are shown in Extended Data Figs. 1–3.

To quantify the morphological variability in the dark oval across observations, we found the best-fitting ellipse for each observation (Methods). We used the best-fitting ellipses to derive time series for the latitude, longitude and area (Fig. 3 and Extended Data Table 1) of the SUDOs, although the ellipse-fitting procedure underestimated the full extent of the dark oval for irregular morphologies, such as those in 2017.25 and 2021.67. Extended Data Fig. 4 shows other ellipse fits of UV-dark ovals (UDOs), including those with irregular morphologies, to show the efficacy of the ellipse-finding algorithm. We quantified the contrast of the dark oval using the optical volume, defined as the area multiplied by the average contrast inside the ellipse.

The centres of the features remained roughly constant at 80° S planetographic latitude and 20° W system III longitude throughout the entire observation window. In fact, all but one detected SUDO were found inside the main auroral oval computed by ref. 8 (cyan outlines in Figs. 1 and 2). The one SUDO outside the auroral oval (2015.05) had the weakest optical volume compared to the other detections, suggesting that the feature was observed in the process of dissipating. The Cassini NUDO spent most of its time inside the auroral oval and decayed quickly after exiting the auroral zone, with contrast weakening after the

feature left the auroral oval (Extended Data Fig. 3 and Supplementary Video 2 of ref. 2).

The previously detected NUDOs were closer to the equator, extending below 60° N, whereas the newly discovered SUDOs never extended above 70° S in all observations. The corresponding auroral ovals are likewise asymmetric; the northern auroral oval extends further equatorwards than the southern one. The area of the dark oval ranged between 0.5 and 2.0×10^8 km^2. This is less than half the size of the Cassini NUDO, which was ~4×10^8 km^2 (ref. 2).

Our time series places constraints on the evolution of SUDOs. A feature developed within the 31 days between 2016.94 and 2017.03. A feature was visible at 2017.03, 2017.09 and 2017.25, consistent with an 82 day minimum lifetime. The non-continuous HST coverage means that we cannot rule out the possibility that separate SUDO features were seen. For comparison, the Cassini NUDO persisted for ~70 days[2,7]. The SUDO detection on 2018.25, followed by a non-detection on 2018.29, indicates that dissipation can occur in as short as 16 days.

Out of the 25 southern observations, 12 contain a SUDO. Although we have non-uniform time sampling, this transient feature appears in 48% of the observations. If we assume that consecutive detections within 120 days represent a single occurrence (based on the Cassini NUDO lifetime), then we detected a SUDO in 8 of 15 observing windows (53%). We detected two NUDOs (1997.71 and 2015.05) in separate observing windows, so the southern features are four to six times more common than their northern counterparts.

Table 1 | HST WFPC2 and WFC3 observations

Decimal date	Proposal ID	Instrument/filter	Start time	End time	Frames	Subobserver latitude	Geocentric distance (AU)	NUDO area (10^8 km²)	SUDO area (10^8 km²)
1994.54	5642	WFPC2/F255W	15 Jul. 1994 12:16	15 Jul. 1994 20:30	9	−3.42	5.11	—	—
1994.65	5642	WFPC2/F255W	24 Aug. 1994 22:20	25 Aug. 1994 05:00	9	−3.32	5.71	—	—
1995.12	5313	WFPC2/F255W	13 Feb. 1995 01:35	13 Feb. 1995 07:56	5	−3.41	5.60	NA[a]	~0.6
1995.76	6009	WFPC2/F255W	4 Oct. 1995 18:49	5 Oct. 1995 14:07	9	−3.00	5.73	—	—
1996.37	6009	WFPC2/F255W	14 May 1996 13:28	14 May 1996 23:19	7	−2.00	4.56	—	NA[a]
1997.71	7430	WFPC2/F255W	18 Sep. 1997 13:57	18 Sep. 1997 22:14	12	0.06	4.27	0.8±0.2	—
1997.85	7430	WFPC2/F255W	6 Nov. 1997 05:53	6 Nov. 1997 14:14	12	0.02	4.94	—	—
1999.61	8148	WFPC2/F255W	11 Aug. 1999 13:49	11 Aug. 1999 22:15	12	3.68	4.61	—	—
1999.78	8148	WFPC2/F255W	14 Oct. 1999 03:52	14 Oct. 1999 12:10	12	3.79	3.97	—	—
2007.15	11096	WFPC2/F255W	26 Feb. 2007 04:26	26 Feb. 2007 13:56	7	−3.31	5.44	—	~0.7
2007.23	11096	WFPC2/F255W	25 Mar. 2007 15:06	26 Mar. 2007 00:36	7	−3.31	5.00	—	~0.6
2012.72	13067	WFC3/F275W	19 Sep. 2012 23:39	20 Sep. 2012 21:04	64	3.44	4.74	—	—
2015.05	13937	WFC3/F275W	19 Jan. 2015 02:38	19 Jan. 2015 23:20	13	−0.26	4.40	0.6±0.2	0.9±0.3
2016.11	14334	WFC3/F275W	9 Feb. 2016 09:59	10 Feb. 2016 05:04	13	−2.21	4.56	—	—
2016.94	14661	WFC3/F275W	11 Dec. 2016 08:07	12 Dec. 2016 08:10	32	−3.03	5.86	—	—
2017.03	14839	WFC3/F275W	11 Jan. 2017 10:55	11 Jan. 2017 23:50	22	−3.27	5.38	—	1.2±0.4
2017.09	14661	WFC3/F275W	1 Feb. 2017 15:37	2 Feb. 2017 12:26	29	−3.40	5.04	—	1.6±0.5
2017.25	14756	WFC3/F275W	3 Apr. 2017 01:33	3 Apr. 2017 22:21	12	−3.46	4.46	—	1.4±0.3
2018.25	14661	WFC3/F275W	1 Apr. 2018 08:50	1 Apr. 2018 23:27	14	−3.87	4.62	—	0.9±0.2
2018.29	15262	WFC3/F275W	17 Apr. 2018 01:37	17 Apr. 2018 20:46	11	−3.88	4.48	—	—
2019.26	15665, 14661, 15159	WFC3/F275W	6 Apr. 2019 10:32	10 Apr. 2019 00:58	17	−3.16	4.86	—	1.0±0.3
2019.48	15502	WFC3/F275W	26 Jun. 2019 08:36	27 Jun. 2019 05:16	13	−3.12	4.31	—	1.2±0.3
2020.56	16053	WFC3/F275W	22 Jul. 2020 05:20	25 Jul. 2020 09:48	12	−1.45	4.15	—	—
2020.65	15929	WFC3/F275W	24 Aug. 2020 22:14	25 Aug. 2020 15:45	13	−1.49	4.37	—	—
2021.67	16266	WFC3/F275W	4 Sep. 2021 01:15	4 Sep. 2021 20:26	13	0.81	4.05	—	1.2±0.4
2022.86	16790	WFC3/F275W	12 Nov. 2022 01:46	12 Nov. 2022 19:14	10	2.63	4.26	—	~0.5

[a]No global coverage of the pole. Dates are grouped into 120 day observation windows as distinct detections. There are 26 dates, with 25 dates per pole separated into 15 windows. For the north pole, 2 out of 15 windows and 2 out of 25 dates show detections. For the south pole, 8 out of 15 windows and 12 out of 25 dates show detections. The areas of the UDOs were approximated by the fitted ellipses (Methods). NA, not applicable.

Aerosols

Figure 4 compares the observed reflectivity to radiative transfer models, with reflectivity given in I/F units (Section 2.7 in ref. 9). Reflectivity versus latitude is plotted for both the SUDO and the background atmosphere, with colours (red and blue) used to represent two fixed central meridian longitude (CML) offsets of 11° and 68°. For the region in which the dark oval is the darkest, the fractional change of I/F is 0.8 for both CML offsets. For the HST SUDO observations, we have detections only in broadband UV filters. Polar methane-band HST images (889 nm) did not reveal corresponding features, even at times when the SUDO was clearly seen in UV data (Extended Data Fig. 5).

Using a combination of Cassini imaging and ground-based near-infrared spectroscopy, ref. 10 retrieved the general properties of haze in Jupiter's stratosphere. They found that the aerosols in the polar region can be explained by aggregated particles with a fractal dimension of two. However, the southern extent of their analysed latitudes was 70° S, whereas SUDOs are usually darkest near 80° S. Stratospheric hazes in the high-latitude polar hood extend to higher altitudes than at lower latitudes and have higher opacity, based on an analysis of Voyager photopolarimeter UV data, ground-based near-infrared spectra, Cassini imaging at UV and methane-band wavelengths, and UV spectra from the Juno UV spectrograph[5,10–12].

In this study, we assumed that the particular properties at higher latitudes were the same as those near 70° S in ref. 10, but we changed the vertical distribution by scaling the haze optical depth and adding an extended haze layer above the 4 mbar level. Several solutions are given in the previous work (Fig. 10 in ref. 10). We adopted the imaginary

part of the refractive index of 0.04 in the UV wavelengths. The retrieved fractal aggregates from the Cassini data are composed of about 120 monomers with a monomer radius of 32.6 nm.

Using the multiple-scattering radiative-transfer model in ref. 10 (Methods), we first fitted the background UV I/F distributions as a function of latitude beyond 70° S for fixed CML offsets of 11° and 68°. The data and models are compared in Fig. 4. We made the simplest assumption that the haze vertical distribution in ref. 10 remained the same as the background within the dark oval, but we varied a uniform scaling factor for the haze abundance at each level until the model output matched the SUDO I/F. We found that a haze enhancement by a factor of 20–50 matched the observed decrease in I/F (Extended Data Fig. 6). In this model, the extended haze layer in the upper stratosphere contributes most to the darkness of the SUDO, whereas lower-altitude haze primarily contributes to the background I/F. Although it is possible that the haze distributions in the SUDO and the background are different, the current data do not provide enough constraints.

Polar vortices

As both NUDOs and SUDOs are generated within Jupiter's auroral ovals, it is clear that these dynamic features are ultimately driven by interactions with the planet's magnetosphere. We hypothesize that momentum, not heating, from the magnetosphere is the ultimate driver of SUDO stratospheric aerosol enhancements. The enhanced aerosols may also provide positive feedback within the polar stratospheric heat budget.
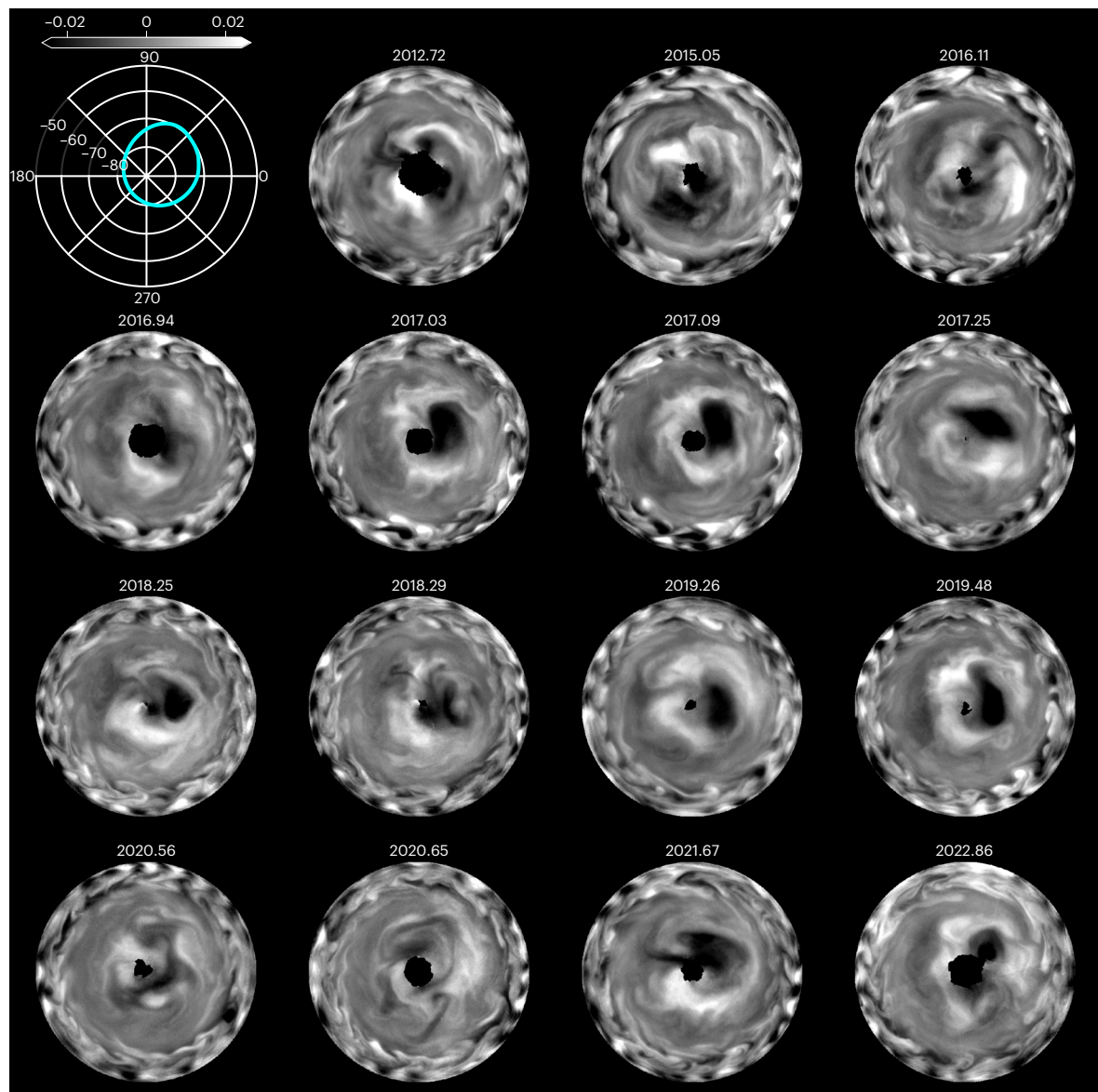
Fig. 2 | South polar maps show well-defined SUDOs for 9 of 15 WFC3 observation dates. Each polar map shows the $\Delta I/F$ (ref. 9), the difference in reflectivity from the zonal average, after the limb-darkening correction and image-stacking described in Methods. The dark oval features have $\Delta I/F < -0.016$ (-1σ). The orthographic coordinate grid for the planetographic latitude and system III longitude is shown in the upper left. Overlaid (cyan) is the auroral oval[8]. See Table 1 for a detailed summary of observations. For the north pole and WFPC2 maps, see Extended Data Figs. 1–3.

A SUDO may represent the continuation of anticyclonic flow detected at higher altitudes in the thermosphere[13], which weakens as it penetrates through the upper stratosphere[14]. When this flow penetrates into the stratospheric aerosol layer, the momentum input affects the aerosol distribution and enables the transient visibility of a SUDO (like a tornado touching down on dusty ground). Table 2 compares the strength of relevant polar vortices situated above and below the SUDO. In the absence of full two-dimensional wind fields, we use the simplifying assumption of solid-body rotation to calculate the vorticity $\zeta = \delta u_\perp / \delta r = u/R$, where we approximate the radial gradient of the horizontal azimuthal velocity $u_\perp$ as the ratio of the characteristic velocity u to the characteristic radius R (ref. 15); refer to Extended Data Fig. 7 and Supplementary Video 1 for a visualization. The sense of the SUDO's rotation is anticyclonic (anticlockwise; $\zeta < 0$ in Table 2). The SUDO vorticity is stronger than in the background flow south of 76° S, but it is in the same anticyclonic sense as the background and opposite to the cyclonic rotation at upper-tropospheric levels traced by cloud features at visible wavelengths[2]. Our vorticity estimates are based on a

small number of tracers and could be improved in the future by measuring two-dimensional wind fields derived from data spanning a longer time series. The UV imaging data also suggest variable meridional flows.

Modelling has shown that the magnetosphere drives flows into the thermosphere that are confined to the auroral region with the vortex approximately focused on the jovimagnetic pole[16,17]. The thermospheric vortex[13] has a comparable rotation rate to the ~10% sub-corotational lag predicted within Jupiter's outer magnetosphere[18]. That is, the thermosphere near 0.1 μbar moves in step with the average sub-co-rotation of Jupiter's outer magnetosphere[13]. However, models alone are not sensitive to the lower boundary of the magnetosphere-driven vortex and typically enforce an arbitrary boundary condition of full co-rotation just below the aurora region (around 0.01 mbar). The more frequent development of SUDO than NUDO features may result from the smaller size of the southern aurora and its closer alignment to the jovigraphic pole. The smaller size of the auroral oval means that the momentum exchange is concentrated in a smaller thermospheric area, whereas the alignment of the magnetic and rotational poles may promote
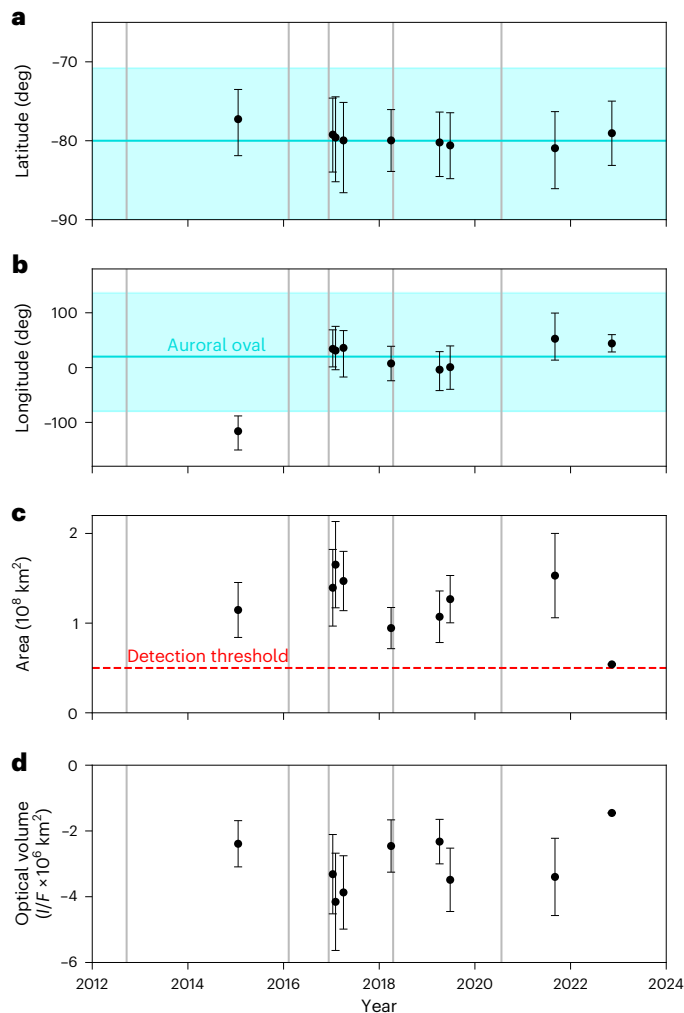
Fig. 3 | Time series of SUDO properties observed by WFC3. a–d, Grey vertical bars denote non-detections. For planetographic latitude (**a**) and longitude (**b**), points denote the calculated centre of the fitted ellipse, and the error bars denote the extent of the ellipse. The cyan lines denote 80° S and 20° W, respectively, for the approximate centre of the southern auroral oval. The shaded cyan regions denote the extent of the auroral oval at the centre. All but one detected SUDO were found entirely inside the oval. For the area (**c**) and optical volume (**d**), the error bars denote errors that were primarily due to pixel resolution (Methods). The points without error bars correspond to 2022.86, for which the subobserver latitude was too high to perform adequate error analysis. The red dashed line represents our threshold value for a dark oval detection. The WFPC2 data do not have sufficiently high resolution to constrain the error, so they are not shown here. See Extended Data Table 1 for the corresponding data.

level (~5–20 mbar) of the SUDO, any direct heating would require the precipitation of highly energetic particles in the >10 MeV range[21]. The temporal and horizontal distributions of the precipitation of deeply penetrating particles correlate poorly with SUDO observations. Deeply precipitating electrons are typically focused on the main auroral oval and the duskward 'active' polar region[22] and are associated with regions of enhanced X-ray aurora[23]. These regions are more fixed in location than the changing location of a SUDO. SUDOs appear to form far more readily than NUDOs, yet X-ray emissions are consistently stronger in the north than the south[23]. In addition, HST auroral observations on 11 December 2016 showed bright active region emission[24], yet we found no SUDO at that time (2016.94 in Fig. 2).

Heating may occur as an effect of the SUDO aerosol enhancement, rather than a driver. Infrared spectroscopic data infer heating near 1 mbar, localized in a spot within the main auroral region, rather than covering the entire oval[20,25]. The 1 mbar hotspot moved between observed events, like the changing location of the SUDO features. Two potential sources for this heating have been suggested[20]: adiabatic heating produced by auroral-driven downwelling confined to pressures >0.1 mbar and short-wave radiation heating of haze or aerosols at the 1 mbar level. Downwelling in the stable stratosphere could drive divergence and, thus, anticyclonic flow at the level of the SUDO, but downwelling would locally suppress aerosol densities in the polar-hood haze layer rather than enhance them. However, if aerosols are mixed upwards by increased turbulence within a broad vortex extending down from the thermosphere, their locally higher opacities would naturally produce heating through absorption of short-wave radiation from both diffuse auroral emissions and solar UV light[26].

Discussion

SUDOs seem to be common features in the polar-hood aerosol layer, with ~50% detection frequencies from 1994 to 2022 (Table 1). In contrast, only three NUDOs have been seen in combined HST and Cassini data. The higher southern occurrence rate may result from concentrated magnetospheric forcing and better alignment between the rotational and magnetic poles.

The UDOs are made visible by changes in aerosol-particle properties and distributions. Our modelling shows that the enhanced SUDO contrast can be explained by an approximately 50× increase in aerosol number density (compared to the background distribution of aerosols in the polar hood). Our HST time-series data are not sufficient to fully constrain the aerosol distribution, so degeneracies persist (particularly between aerosol density and altitude level). Future observations with expanded temporal, spectral or phase angle coverage may be able to better constrain the specific aerosol properties responsible for the enhanced contrast in UDOs.

The results of previous studies are consistent with a scenario in which enhanced turbulent mixing in the SUDO causes increased aerosol concentrations by bringing material up from deeper levels. Aerosol absorption of short-wave radiation within the SUDO would establish positive feedback through localized heating. Direct heating by particle precipitation is not considered to be a primary mechanism because our models fit SUDO reflectivities using aerosols in the 1–20 mbar range. These levels can be reached by only the most energetic particles, but high-energy particle precipitation differs from the morphological and temporal characteristics that we measured for SUDOs[21–24]. Instead, our observations of the SUDO rotation rate suggest it is a deep extension of the polar vortex at the thermosphere and upper stratosphere levels, driven by ion–neutral momentum exchange and forced by subrotating field lines experiencing Keplerian drag in the Jovian system[13].

The increased aerosol opacity in our radiative-transfer analysis (Fig. 4 and Extended Data Fig. 6) falls in the 1–10 mbar range, where aerosol formation due to condensation of polycyclic aromatic hydrocarbons is effective[27], particularly in the auroral regions[28]. Ion–neutral chemistry has been invoked to explain observations of increased

deep vortex penetration due to a simpler background horizontal shear environment (compared to the north, where the magnetic and rotational poles are more offset). Indeed, ref. 14 showed that the southern auroral winds near 0.1 mbar were much stronger than their northern counterparts. Magnetosphere-driven flows probably remain stable against varying auroral power, as the ion drag acceleration is weak in Jupiter's thermosphere[19]. Thus, the changing location and dynamics seen in the relatively deep SUDO result from the remoteness of the magnetospheric driver of these winds and the unknown dynamics within the stratosphere affecting the penetration level of the thermospheric vortex.

Heating occurs in the stratospheric auroral region, but its distribution suggests that heating is not the main driver for SUDOs. Most auroral energy deposition is modelled[19] and measured[20] to fall in the upper stratosphere around 0.01 mbar, well above the SUDO. At the deep
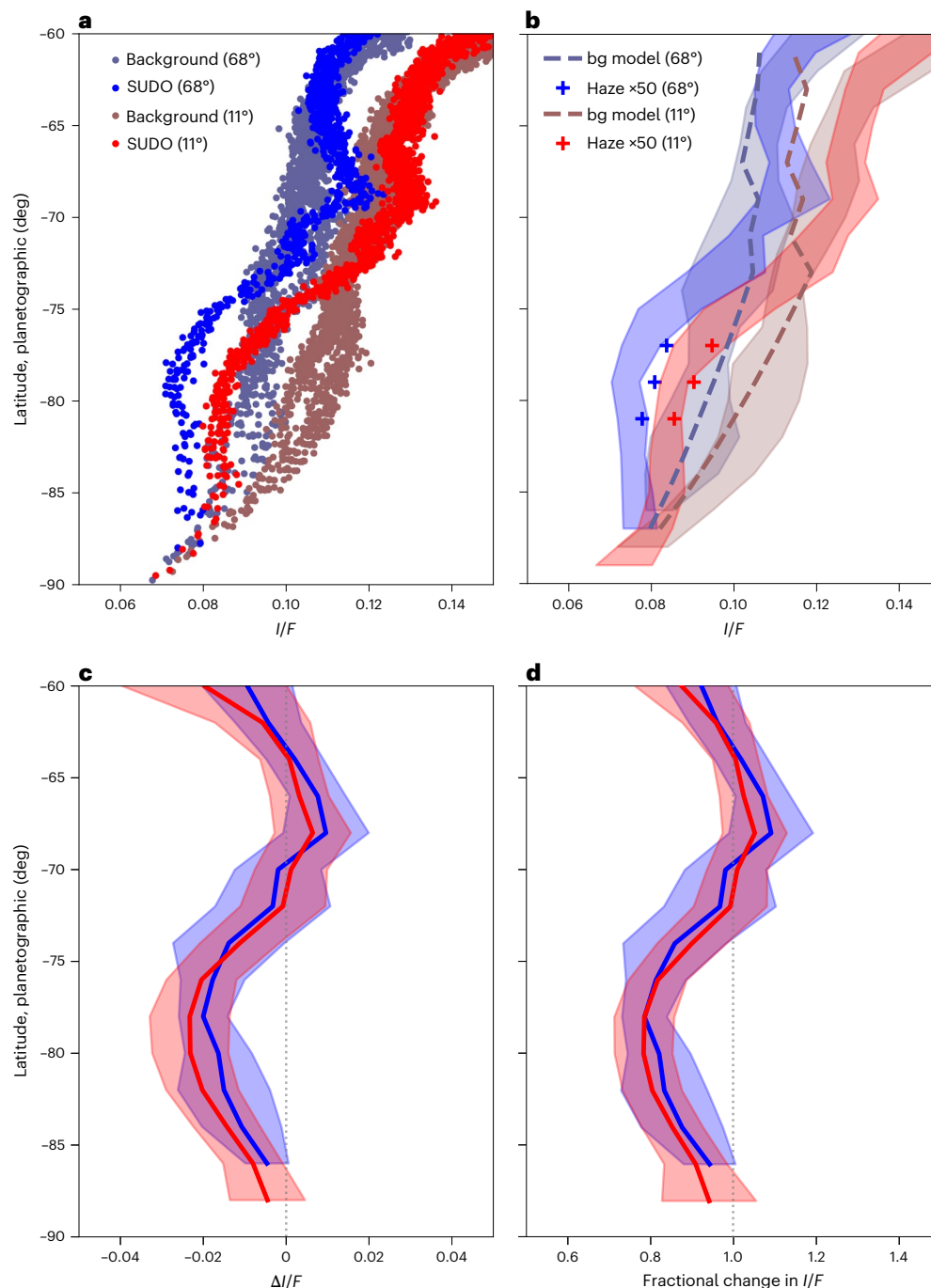
Fig. 4 | Reflectivity versus latitude is modelled as an enhancement of stratospheric haze. a–d, A decrease in 275 nm I/F in the dark oval was observed for fixed CML offsets of 11.3° (red) and 68.4° (blue) at a phase angle of 9.8°. Bright data denote dark oval data, and greyed-out data denote background data with no dark oval on the same observing date (2017.09). **a**, Raw data for the background and dark oval. **b**, Shaded regions denote ±2 standard deviations of the data in **a** in increments of 2° latitude. Dashed lines denote the background I/F values given by the aerosol model from ref. 10 with an imaginary index of refraction of 0.04. Bright markers reflect the modelled I/F value in the dark oval due to a 50 times

increase in haze abundance. **c**, Difference between raw data and background, denoted $\Delta I/F$. Note that here we define $\Delta I/F$ as the difference between oval and background reflectivity, whereas elsewhere in the paper we define it as the difference between the reflectivity in each map pixel and the zonal mean. The shaded region is the combined error from both the raw data and background. The dotted line denotes no deviation from background. **d**, Fractional change between the dark oval and background, which was about 0.8 at the darkest point for both CML offsets. bg, background.

stratospheric benzene concentrations in the polar regions[29] and even higher concentrations in the auroral regions[30]. The polycyclic aromatic hydrocarbon pathway for aerosol production in the 1–10 mbar range has a condensation time constant of about 12 days[31], which is comparable to our constraints that SUDOs may develop within 30 days or less and dissipate in 16 days or less.

UDOs represent a new line of investigation into interactions between Jupiter's magnetosphere and atmosphere, as they are visible in scattered solar near-UV light rather than the more familiar auroral emission in far-UV light. Differences between NUDO and SUDO occurrence rates suggest that the more concentrated field geometry in the south (and better magnetic–rotational pole alignment) facilitates the

Table 2 | Polar vortices of Jupiter

Layer/feature	Pressure (mbar)	Vorticity (s^{-1})
Thermosphere	10^{-4}	−1.2×10^{-4}
Stratosphere (south)	0.1	−2×10^{-5}
SUDO	2–20	−3×10^{-6}
NUDO	2–20	−4×10^{-6}
Stratosphere (south)	20	−8×10^{-7}
Cloud tops (south)	500–800	+2×10^{-7}

The vorticity of the thermospheric vortex was calculated using $u=-1.5\,km\,s^{-1}$ measured from H_2 quadrupole emission and $R=12,500\,km$ (7″ diameter)[13]. The vorticity of the 0.1 mbar stratospheric polar vortex was calculated using $u=-300\,m\,s^{-1}$ measured from HCN Doppler shifts using data from the Atacama Large Millimeter Array[14], and $R=18,000\,km$ for the auroral oval. The SUDO vorticity was calculated using a 590 h anticyclonic rotation period estimated from 9.9 h separated HST data (2017.09), and $R≈7,100\,km$ corresponding to the feature area (Table 1); see Extended Data Fig. 7 and Supplementary Video 1 for a visualization. The NUDO vorticity was calculated with an 18 Earth day period and $R≈9,000\,km$ using Cassini data analysed by ref. 40. The vorticity of the 20 mbar stratospheric polar vortex was calculated using $u=-13\,m\,s^{-1}$ at 76° S from 29.8 h separated HST UV data (2019.26), assuming a linear decay to zero at the pole. The vorticity of the tropospheric polar vortex was calculated using $u=+3\,m\,s^{-1}$ at 76° S from the smoothed Cassini zonal wind profile[2], assuming a linear decay to zero at the pole.

transfer of momentum from the thermospheric polar vortex. Determining the primary cause of aerosol enhancements in NUDOs and SUDOs—vertical mixing of pre-existing particles or increased aerosol production in the auroral region—will require future studies, such as time-series measurements of localized benzene concentration from 14.8 μm spectroscopy, time-series UV spectral scans and aerosol retrievals, magnetohydrodynamical simulations of the momentum transport from the thermosphere to the deep stratosphere and accurate measurements of wind fields at several levels.

Methods

Observations

We analysed HST data from 26 dates between 1994 and 2022 with a global coverage of Jupiter on UV filters. Data for 11 dates were collected by the WFPC2 F255W filter between 1994 and 2007, and data for the remaining 15 were collected by the WFC3 F275W filter between 2012 and 2022. Select dates also have images from the 225 and 889 nm filters, which we used for an extra analysis (Extended Data Fig. 5). Further observation details are listed in Table 1, which gives the programme IDs that can be used to retrieve the data from the HST archive. Programme IDs 13937, 14334, 14756, 15262, 15502, 15929, 16266 and 16790 are from the Outer Planet Atmospheres Legacy programme[32], which conducts observations close to solar opposition to maximize the spatial resolution on Jupiter.

Data processing

The UDOs are not immediately evident from raw HST data because the ovals are a relatively low-contrast phenomenon within the high-contrast dark polar hoods and because limb-darkening also has a strong effect. Our image-processing pipeline is illustrated in Fig. 1. There are five main parts to the preparation: navigation, polar projection, stacking, limb-darkening correction and average subtraction.

First, we cleaned the raw data and navigated the images into high-level science products containing backplanes for latitude, longitude, emission angle and solar incidence angle. For the WFC3 data, we calibrated the image data in I/F reflectivity units[9] using the latest time-dependent photometry[33]. WFPC2 data were retrieved from the archive in 2023 and were processed with v.2.5.3 of the CALWP2 pipeline[34]. The WFPC2 data were acquired when the disk of Jupiter fell onto one to four detectors, which have different resolutions. Each detector frame was individually navigated using the same approach as for the WFC3 data. Navigation uncertainty is higher when only a small portion of the disk was visible on any one of the four detectors in WFPC2.

Then, we performed orthographic north and south polar projections for each image. We stacked the polar projections together into a global map. Although we have data for several Jupiter rotations for some dates, we stacked all frames into one global map for the primary analysis. This improved resolution and accuracy near the pole but prevented an analysis of short-timescale dynamics. In some cases, such as the analysis of the rotation rate, we used stacks from individual HST orbits (two or three images each).

We then used a first-order Minnaert function to correct for limb-darkening and improve the contrast between the dark oval and background (equation (1) in ref. 35). For each HST orbit, we computed the optimal Minnaert parameter k by finding the value that minimizes the squared residuals against a straight-line fit at a fixed planetographic latitude of ±70°. This latitude lies inside the northern and southern polar hoods. Generally, we found that $k = 0.68 ± 0.01$ worked well for most observations. We applied the Minnaert correction to the global maps.

Last, we computed the zonal mean I/F value using the Minnaert-corrected data for each date and subtracted the zonal mean profile from the global map. We defined $\Delta I/F$ to be the difference between the observed I/F value and the zonal mean.

Analysis

A pixel in the polar map was considered to be 'inside the dark spot' if the Minnaert-corrected average-subtracted I/F value was less than −0.016 or roughly one standard deviation from the mean. After classifying the pixels in this manner, we found the best-fitting ellipse for the dark spot by maximizing the area. A valid ellipse has at least 98% of its pixels below the cutoff I/F value to account for pixel-to-pixel noise and missing data near the pole.

We found ellipses for each observation but set one criterion to determine a dark oval detection: the area must be at least $5 × 10^7\,km^2$. This cutoff was set a posteriori after we had compared visual results in the polar maps. Some polar maps seem to have incomplete or weak dark spots that do not satisfy this criterion (2016.94 and 2018.29 in Fig. 2); therefore, we may have underestimated the frequency of UDOs.

To determine the error in the ellipse area for WFC3 observations, we used the full-width at half-maximum of 0.077 arcsec of the point spread function for the F275W filter[36]. We converted this to latitude and longitude resolutions. The WFPC2 detection of a NUDO in 1997.71 (the only full UDO seen with WFPC2) was made with the WF3 detector, whose 0.1″ pixel size does not critically sample the point spread function[34], so we used 0.1″ to estimate the resolution error. Using these resolutions, we computed the error of the axes of the ellipse and propagated this error into the area.

We accounted for several factors that varied between observations. First, the geocentric distance varied between 4 and 6 AU. Second, the subobserver latitude ranged between −4° and 4°, which had a notable effect on the latitude resolution and visual coverage near the pole. This may have limited the rigorous analysis, as demonstrated in the SUDO detections on 1995.12, 2007.15, 2007.23 and 2022.86. In these cases, we were still able to detect a dark oval visually, but the feature intersected the gap in the data close to the pole, so the area could not be reliably determined.

The dark ovals did not necessarily appear at the CML. As the CML offset increased, the longitude resolution degraded. However, our global maps were optimized for the lowest emission angles nearest to the central meridian in the stacked frames. For the error estimation, we took the resolution at the CML offset of ±15° to be representative.

Last, the latitude selected to determine the resolution had a notable effect. We took the resolution at 80° S to be representative, although we recognize that the error near the edge of the visual coverage at the pole was not negligible. Other sources of error during processing, including the limb-darkening correction, were negligible compared to the aforementioned resolution error.

Aerosol radiative-transfer modelling

Our haze radiative-transfer model was taken from the forward model in ref. 10, which is based on the multiple-scattering radiative-transfer solver DISORT[37,38]. We used 32 streams to characterize the angular distribution of the intensity of the scattered light. Our Jupiter model includes CH_4 absorption, Rayleigh scattering and scattering by aerosols and clouds. The model was discretized into 12 vertical atmospheric layers composed of gas and haze in the stratosphere and an 'effective cloud layer' at the bottom to represent the upper-tropospheric clouds. This effective cloud layer, which included all gas and aerosol contributions, was characterized by a single-scattering albedo and a double Henyey–Greenstein phase function (Table 2 in ref. 10).

As we were focused primarily on the SUDO latitudes beyond 70° S where the retrieval data are not available in ref. 10, we assumed that the properties of the haze particles were the same as those at 70° S. The retrieved haze parameters have non-unique solutions in ref. 10. The imaginary part of the UV refractive index ranged from 0.006 to 0.08 for latitude 60° S. For 70° S, the range was narrower, from 0.01 to 0.04. Because SUDOs are dark, stronger UV absorption was preferred. We took the UV imaginary part as 0.04 for all polar latitudes. Based on the vertical profile of the near-infrared optical depth of the haze and the Cassini data for three channels (CB3, MT3 and UV1), the retrieved fractal aggregates at 70° S were composed of about 120 monomers with a monomer radius of 32.6 nm (ref. 10). The vertical distribution of the optical thickness of the haze at each layer is shown in Extended Data Fig. 6.

We assumed all polar latitudes shared the same vertical distribution of the optical depth of the haze beyond 70° S. However, the vertical profile could be different from that at 70° S. To allow some change to the vertical profile despite the poorly constrained nature of the problem, we applied two scaling factors to the vertical distribution of the haze at 70° S. The first one was the scaling of the entire profile. The second factor was specifically applied to the top model layer at 4 mbar. We performed a grid search of the two scaling factors to fit the background UV I/F distributions as a function of latitude beyond 70° S for fixed CML offsets of 11° and 68°. The best-fitting optical depth from this simple scaling model is shown as the black line in Extended Data Fig. 6. The general optical depth was about one-third of that at 70° S, but the top haze layer above 4 mbar was much thicker.

To explain the SUDO, we scaled the profile of the optical depth of the haze profile by a multiplier. A thicker haze resulted in a lower I/F, as absorption by the haze dominated Rayleigh scattering. As shown in Extended Data Fig. 6, a factor of 20–50 increase in the optical depth of the haze may be needed to explain the SUDO data, although further increasing the haze abundance did not result in a lower I/F because it was primarily limited by the single-scattering albedo of the haze. In this model, the I/F of the SUDO is mainly controlled by the top haze layer, whereas the I/F for the background comes from both the top haze layer and lower-altitude haze. Our data do not provide enough constraints on whether the vertical profiles of the haze are different between the SUDO and the background, so we cannot exclude that possibility.

Data availability

Raw and calibrated HST images are available by searching the MAST archive, https://mast.stsci.edu. Polar mosaics and other high-level science products are available from https://doi.org/10.17909/dkep-y451 (ref. 39).

References

1. Simon, A. A., Wong, M. H., Sromovsky, L. A., Fletcher, L. N. & Fry, P. M. Giant planet atmospheres: dynamics and variability from UV to near-IR Hubble and adaptive optics imaging. *Remote Sens.* **14**, 1518 (2022).
2. Porco, C. C. et al. Cassini imaging of Jupiter's atmosphere, satellites, and rings. *Science* **299**, 1541–1547 (2003).
3. West, R. A. Spatially resolved methane band photometry of Jupiter. I. Absolute reflectivity and center-to-limb variations in the 6190-, 7250-, and 8900-Å bands. *Icarus* **38**, 12–33 (1979).
4. Vincent, M. B. et al. Jupiter's polar regions in the ultraviolet as imaged by HST/WFPC2: auroral-aligned features and zonal motions. *Icarus* **143**, 205–222 (2000).
5. Hord, C. W. et al. Photometric observations of Jupiter at 2400 angstroms. *Science* **206**, 956–959 (1979).
6. Pryor, W. R. & Hord, C. W. A study of photopolarimeter system UV absorption data on Jupiter, Saturn, Uranus, and Neptune: implications for auroral haze formation. *Icarus* **91**, 161–172 (1991).
7. West, R. A. et al. in *Jupiter: The Planet, Satellites and Magnetosphere* (eds Bagenal, F. et al.) 79–104 (Cambridge Univ. Press, 2004).
8. Nichols, J. D. et al. Response of Jupiter's auroras to conditions in the interplanetary medium as measured by the Hubble Space Telescope and Juno. *Geophys. Res. Lett.* **44**, 7643–7652 (2017).
9. Wong, M. H. et al. High-resolution UV/optical/IR imaging of Jupiter in 2016-2019. *Astrophys. J. Suppl. Ser.* **247**, 58 (2020).
10. Zhang, X., West, R. A., Banfield, D. & Yung, Y. L. Stratospheric aerosols on Jupiter from Cassini observations. *Icarus* **226**, 159–171 (2013).
11. Banfield, D., Conrath, B. J., Gierasch, P. J., Nicholson, P. D. & Matthews, K. Near-IR spectrophotometry of Jovian aerosols— meridional and vertical distributions. *Icarus* **134**, 11–23 (1998).
12. Giles, R. S. et al. Meridional variations of C_2H_2 in Jupiter's stratosphere from Juno UVS observations. *J. Geophys. Res.* **126**, e2021JE006928 (2021).
13. Wang, R. et al. Asymmetric ionospheric jets in Jupiter's aurora. *J. Geophys. Res.* **128**, e2023JA031861 (2023).
14. Cavalié, T. et al. First direct measurement of auroral and equatorial jets in the stratosphere of Jupiter. *Astron. Astrophys.* **647**, L8 (2021).
15. Vallis, G. K. *Essentials of Atmospheric and Oceanic Dynamics* (Cambridge Univ. Press, 2019).
16. Achilleos, N. et al. JIM: a time-dependent, three-dimensional model of Jupiter's thermosphere and ionosphere. *J. Geophys. Res.* **103**, 20089–20112 (1998).
17. Millward, G., Miller, S., Stallard, T., Achilleos, N. & Aylward, A. D. On the dynamics of the Jovian ionosphere and thermosphere. IV. Ion-neutral coupling. *Icarus* **173**, 200–211 (2005).
18. Cowley, S. W. H., Bunce, E. J., Stallard, T. S. & Miller, S. Jupiter's polar ionospheric flows: theoretical interpretation. *Geophys. Res. Lett.* **30**, 1220 (2003).
19. Tao, C., Fujiwara, H. & Kasaba, Y. Neutral wind control of the Jovian magnetosphere-ionosphere current system. *J. Geophys. Res.* **114**, A08307 (2009).
20. Sinclair, J. A. et al. Jupiter's auroral-related stratospheric heating and chemistry. I. Analysis of Voyager-IRIS and Cassini-CIRS spectra. *Icarus* **292**, 182–207 (2017).
21. Houston, S. J. et al. Jovian auroral ion precipitation: X-ray production from oxygen and sulfur precipitation. *J. Geophys. Res.* **125**, e2019JA027007 (2020).
22. Gérard, J. C. et al. Concurrent ultraviolet and infrared observations of the north Jovian aurora during Juno's first perijove. *Icarus* **312**, 145–156 (2018).
23. Dunn, W. R. in *Handbook of X-ray and Gamma-ray Astrophysics* (eds Bambi, C. & Santangelo, A.) 110 (Springer, 2022).
24. Grodent, D. et al. Jupiter's aurora observed with HST during Juno orbits 3 to 7. *J. Geophys. Res.* **123**, 3299–3319 (2018).
25. Sinclair, J. A. et al. Jupiter's auroral-related stratospheric heating and chemistry. II. Analysis of IRTF-TEXES spectra measured in December 2014. *Icarus* **300**, 305–326 (2018).

26. Sinclair, J. A. et al. Spatial variations in the altitude of the CH_4 homopause at Jupiter's mid-to-high latitudes, as constrained from IRTF-TEXES spectra. *Planet. Sci. J.* **1**, 85 (2020).

27. Lebonnois, S. Benzene and aerosol production in Titan and Jupiter's atmospheres: a sensitivity study. *Planet. Space Sci.* **53**, 486–497 (2005).

28. Wong, A.-S., Yung, Y. L. & Friedson, A. J. Benzene and haze formation in the polar atmosphere of Jupiter. *Geophys. Res. Lett.* **30**, 1447 (2003).

29. Kim, S. J., Caldwell, J., Rivolo, A. R., Wagener, R. & Orton, G. S. Infrared polar brightening on Jupiter. III. Spectrometry from the Voyager 1 IRIS experiment. *Icarus* **64**, 233–248 (1985).

30. Sinclair, J. A. et al. Jupiter's auroral-related stratospheric heating and chemistry. III. Abundances of C_2H_4, CH_3C_2H, C_4H_2 and C_6H_6 from Voyager-IRIS and Cassini-CIRS. *Icarus* **328**, 176–193 (2019).

31. Wong, A.-S., Lee, A. Y. T., Yung, Y. L. & Ajello, J. M. Jupiter: aerosol chemistry in the polar atmosphere. *Astrophys. J.* **534**, L215–L217 (2000).

32. Simon, A., Wong, M. H. & Orton, G. S. First results from the Hubble OPAL program: Jupiter in 2015. *Astrophys. J.* **812**, 55 (2015).

33. Calamida, A. et al. *New Time-Dependent WFC3 UVIS Inverse Sensitivities* Instrument Science Report WFC3 2021-4 (STScI, 2021).

34. McMaster, M. & Biretta, J. *Wide Field and Planetary Camera 2 Instrument Handbook v.10.0* (STScI, 2008).

35. Wong, M. H. et al. A new dark vortex on Neptune. *Astron. J.* **155**, 117 (2018).

36. Dressel, L. & Marinelli, M. *WFC3 Instrument Handbook for Cycle 31 v.15.0* (STScI, 2023).

37. Stamnes, K., Tsay, S. C., Jayaweera, K. & Wiscombe, W. Numerically stable algorithm for discrete-ordinate-method radiative transfer in multiple scattering and emitting layered media. *Appl. Opt.* **27**, 2502–2509 (1988).

38. Buras, R., Dowling, T. & Emde, C. New secondary-scattering correction in DISORT with increased efficiency for forward scattering. *J. Quant. Spectrosc. Radiat. Transf.* **112**, 2028–2034 (2011).

39. Tsubota, T. K. & Wong, M. H. Jupiter UV-dark ovals ('JUDO'). *MAST* https://doi.org/10.17909/dkep-y451 (2024).

40. Barbara, J. M., West, R. A., Del Genio, A. D. & Sinclair, J. A. A study of Jupiter's UV Great Dark Spot and tropopause to stratosphere winds in the high northern latitudes as seen by Cassini imaging. *Icarus* **410**, 115913 (2024).

Author contributions

T.K.T. led the project, processed the HST dataset, constructed the oval morphology analysis pipeline, created the figures, made the data archive and wrote the paper. M.H.W. conceived the project, calibrated the HST data, measured the SUDO vorticity and wrote the discussion. T.S. provided the magnetospheric interpretation of the polar vortices and contributed the associated manuscript text. X.Z. performed the radiative-transfer modelling and contributed the associated manuscript text. A.A.S. assisted with collecting HST/WFPC2 and Outer Planet Atmospheres Legacy data.

Competing interests

The authors declare no competing interests.

Additional information

Extended data is available for this paper at https://doi.org/10.1038/s41550-024-02419-0.

Supplementary information The online version contains supplementary material available at https://doi.org/10.1038/s41550-024-02419-0.

Correspondence and requests for materials should be addressed to Troy K. Tsubota or Michael H. Wong.
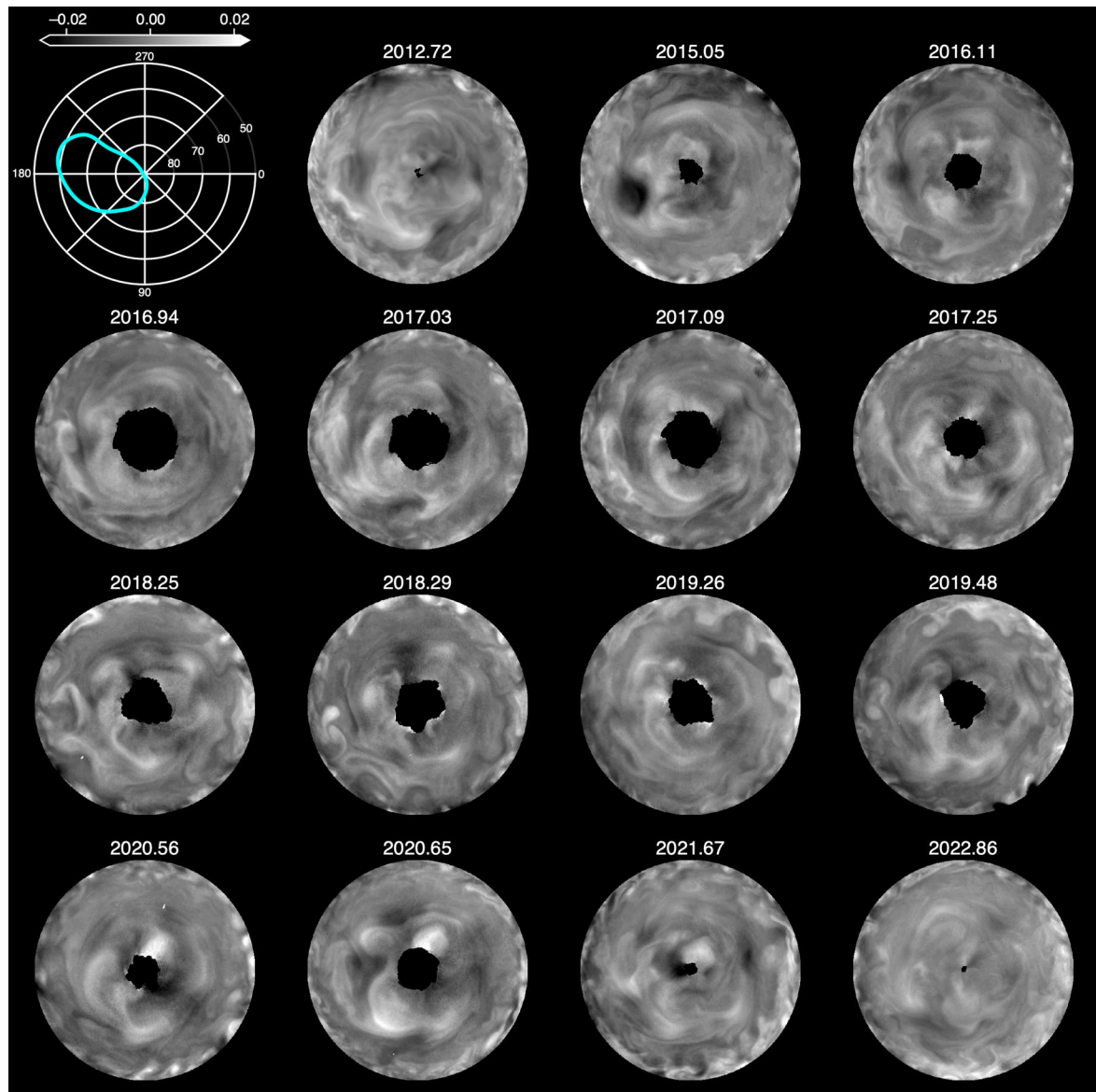
Peer review information *Nature Astronomy* thanks the anonymous reviewers for their contribution to the peer review of this work.

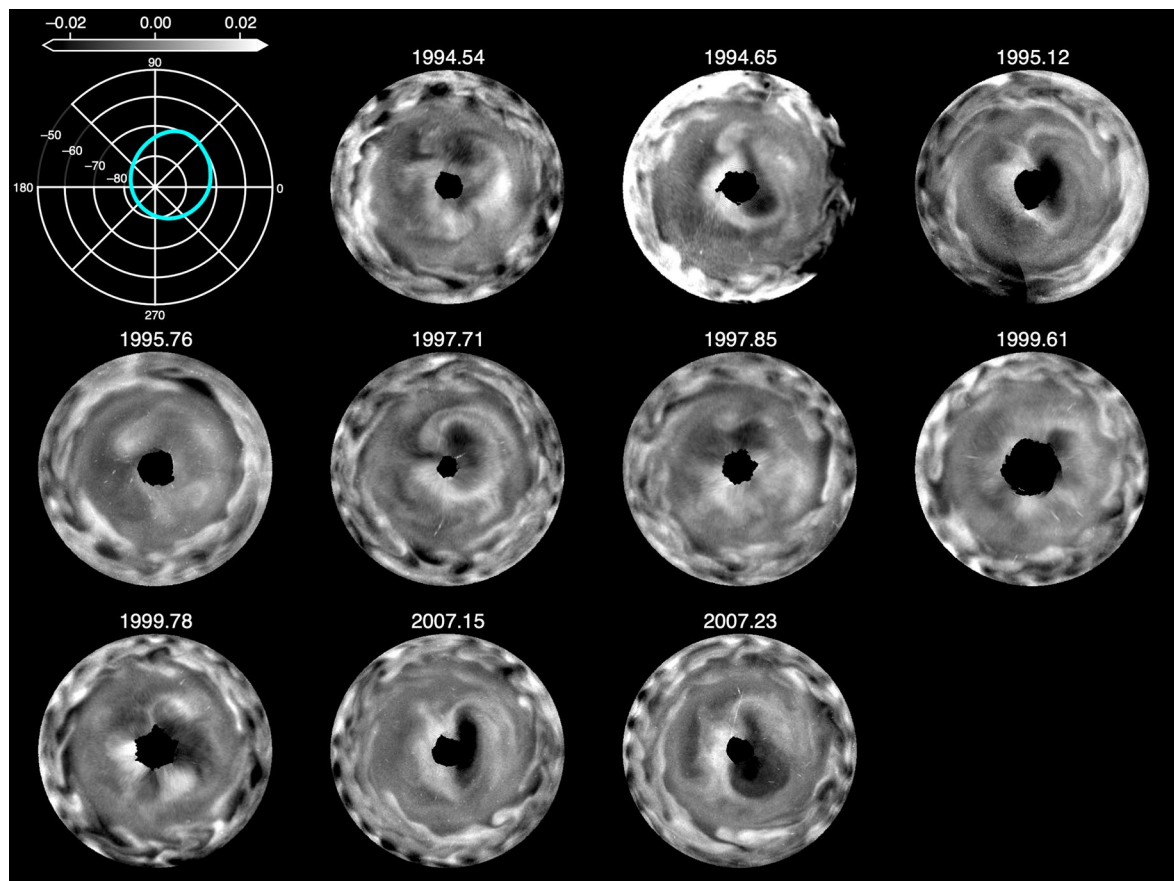**Reprints and permissions information** is available at www.nature.com/reprints.

Extended Data Fig. 1 | HST/WFC3 F275W north pole maps. North polar maps show one NUDO present in fifteen WFC3 observation dates. Refer to Fig. 2 and Methods for detection criteria.

Extended Data Fig. 2 | HST/WFPC2 F255W south pole maps. South polar maps show SUDOs present in 3 of 10 WFPC2 observation dates. Refer to Fig. 2 and Methods for detection criteria.
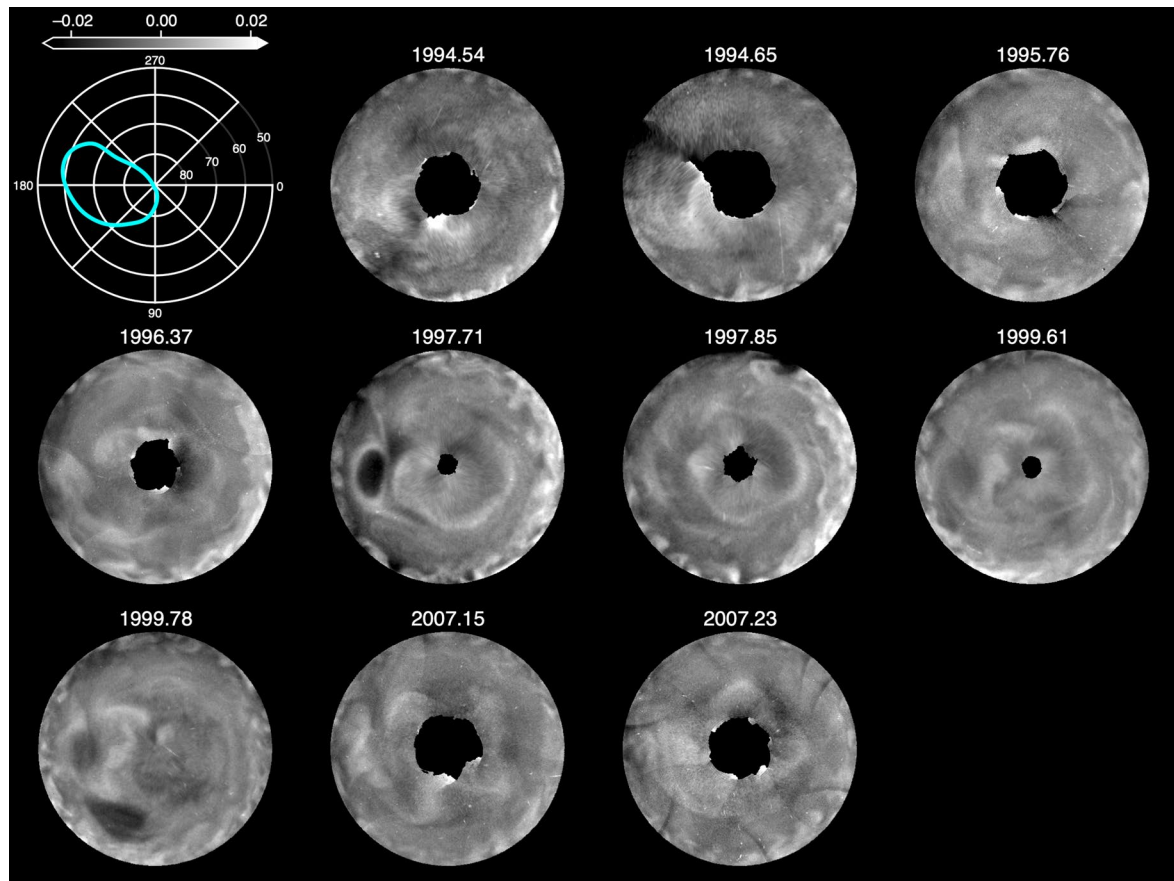
Extended Data Fig. 3 | HST/WFPC2 F255W north pole maps. North polar maps show one NUDO present in ten WFPC2 observation dates. Refer to Fig. 2 and Methods for detection criteria.
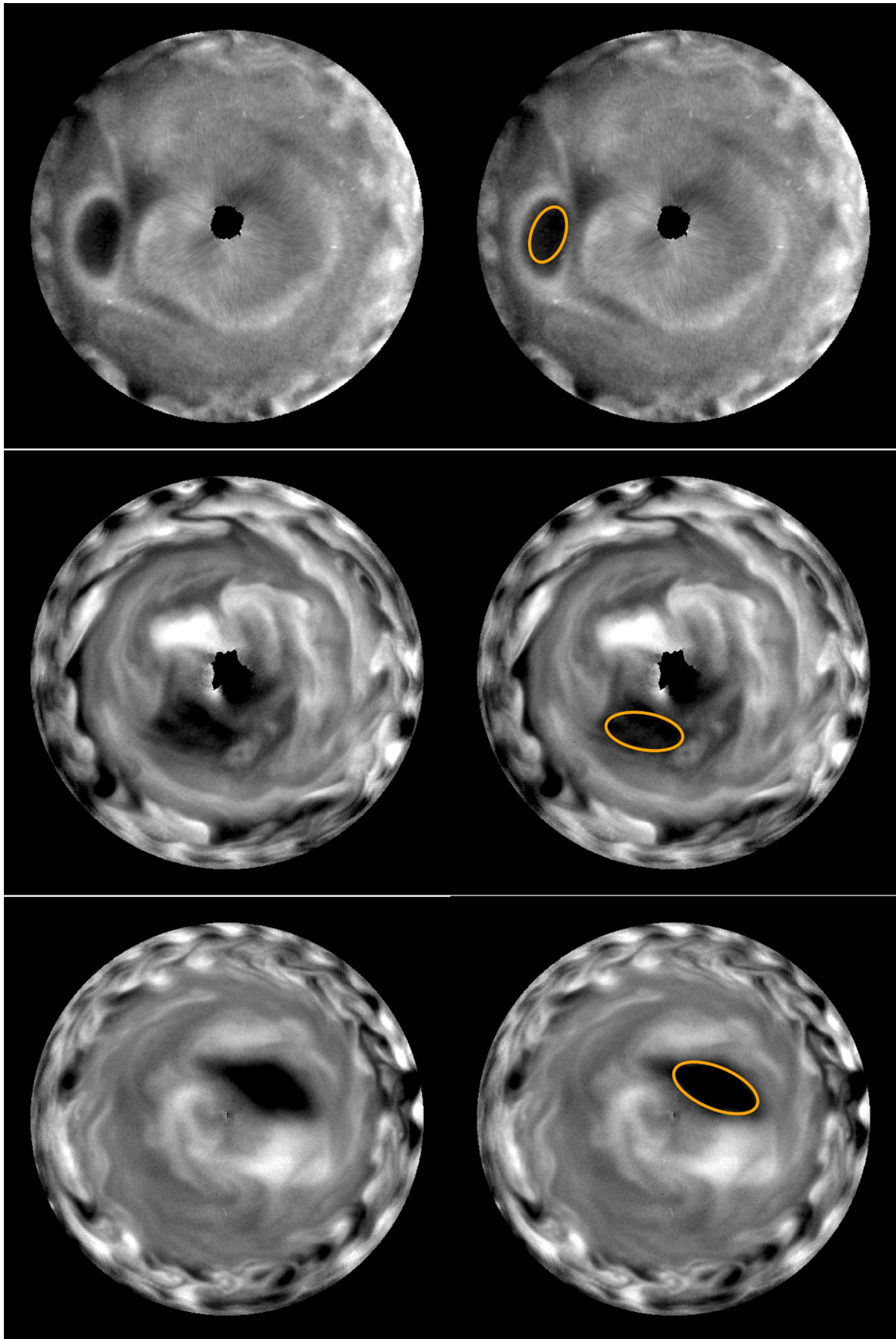
Extended Data Fig. 4 | Additional ellipse fits. Additional ellipse fits for the 1997.71 NUDO, 2015.15 SUDO, and 2017.25 SUDO.
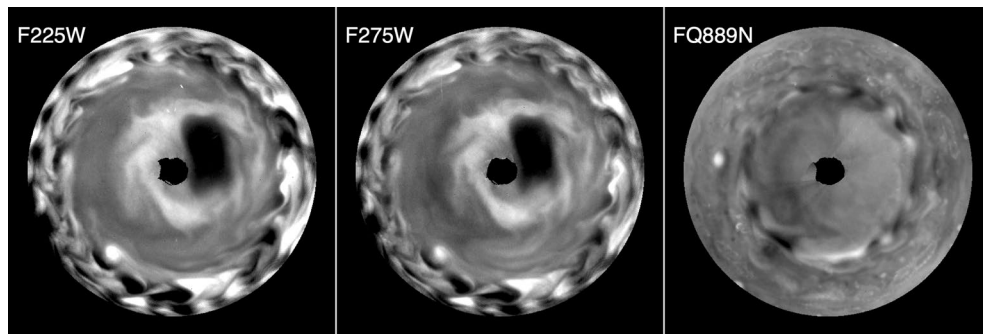
Extended Data Fig. 5 | SUDO in different wavelengths. South polar maps of the 2017.09 observations with the F225W, F275W, and FQ889N filters. The F225W and F275W UV-band filters show very similar results. The FQ889N methane-band filter does not show a SUDO detection despite its detection in the UV.
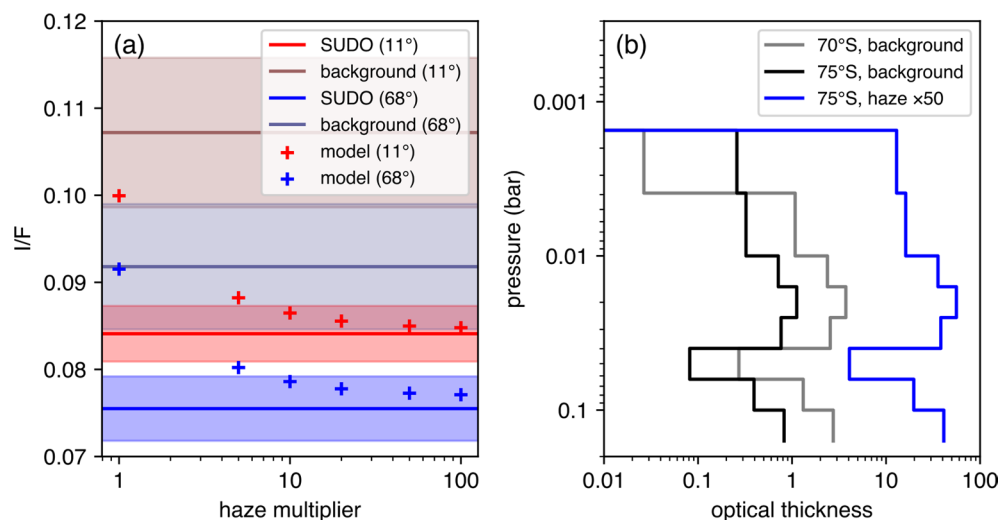
Extended Data Fig. 6 | Radiative transfer model details. Radiative transfer model for 81°S. Subfigure (**a**) compares the observed I/F values (horizontal lines, error bars shaded) to the model I/F values (scatter points) at different haze multipliers relative to baseline. The shaded error is the same as that for 81° latitude in Fig. 4b. Blue and red correspond to 68° and 11° CML offsets, respectively. The grayed out lines denote the observed background, while the bright lines denote the observed SUDO I/F. Subfigure (**b**) shows the optical thickness over pressure for the 70°S background (gray), 75°S background (black), and the ×50 haze model at 75°S (blue).
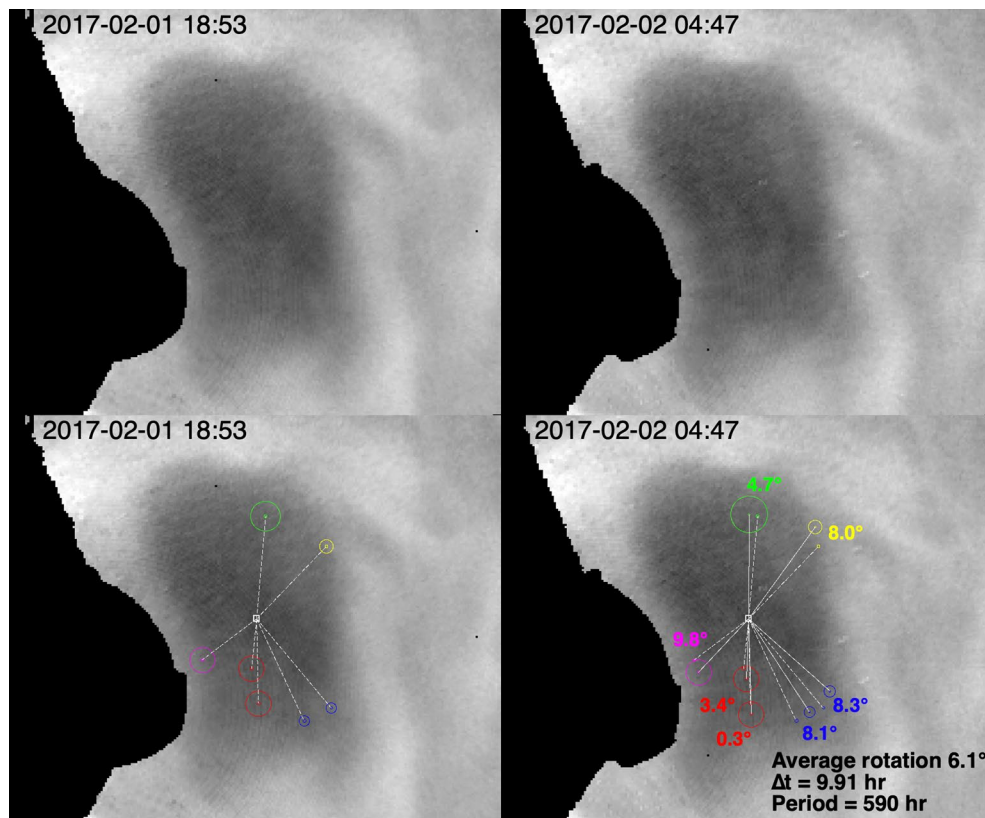
Extended Data Fig. 7 | SUDO rotation measurement. To estimate the rotation of the SUDO, we manually identified seven low-contrast tie points in the 2017.09 data. Using the area of 1.6×10^8 km² (Table 1), we estimate a characteristic radius R of 7100 km, which gives a characteristic tangential wind speed of 21 m/s for a period of 590 hours. The vorticity is then $u/R = -3 \times 10^{-6}$ s⁻¹ (negative for anticyclonic rotation). Top row: polar maps at 275 nm, separated by 9.9 hours.

Bottom row: Colored circles indicate manual tracking tie points, with angular displacements relative to the SUDO center (white square; see Extended Data Table 1) labeled in matching color. The angular displacements were measured by comparing the dashed and solid white line segments in the lower right panel. An animated version of this figure is available as a Supplementary Video.

Extended Data Table 1 | WFC3 SUDO time series

Date	Latitude[1] center (min, max)	Longitude[2] center (min, max)	Oval Area (10^8 km^2)	Optical Volume (10^6 $I/F \cdot$ km^2)
2012.72	—	—	—	—
2015.05	-77.3 $(-81.0, -72.6)$	-116 $(-144, -82)$	1.1 ± 0.3	-2.4 ± 0.7
2016.11	—	—	—	—
2016.94	—	—	—	—
2017.03	-79.2 $(-83.9, -74.5)$	34 $(-1, 67)$	1.4 ± 0.4	-3.3 ± 1.2
2017.09	-79.6 $(-84.7, -74.0)$	31 $(-13, 66)$	1.7 ± 0.5	-4.2 ± 1.5
2017.25	-80.0 $(-84.8, -73.3)$	36 $(-4, 89)$	1.5 ± 0.3	-3.9 ± 1.1
2018.25	-80.0 $(-83.9, -76.0)$	7 $(-24, 39)$	0.9 ± 0.2	-2.5 ± 0.8
2018.29	—	—	—	—
2019.26	-80.2 $(-84.1, -75.9)$	-4 $(-37, 34)$	1.1 ± 0.3	-2.3 ± 0.7
2020.56	—	—	—	—
2020.65	—	—	—	—
2021.67	-81.0 $(-85.6, -75.8)$	53 $(6, 92)$	1.5 ± 0.5	-3.4 ± 1.2
2022.86	~ -79	~ 44	~ 0.5	~ -1.5

[1]Planetographic latitude (degrees).

[2]System III longitude defined between $-180°$ and $180°$.

The time series data are derived from the ellipse fits.